

Blowing star formation away in AGN Hosts (BAH) - I. First Observation of Warm Molecular Outflows with JWST MIRI

J. H. COSTA-SOUZA ¹, ROGEMAR A. RIFFEL ¹, GABRIEL L. SOUZA-OLIVEIRA ¹, NADIA L. ZAKAMSKA ²,
MARINA BIANCHIN ³, THAISA STORCHI-BERGMANN ⁴, AND ROGÉRIO RIFFEL ⁴

¹*Departamento de Física, CCNE, Universidade Federal de Santa Maria, Av. Roraima 1000, 97105-900, Santa Maria, RS, Brazil*

²*Department of Physics & Astronomy, Johns Hopkins University, Bloomberg Center, 3400 N. Charles St, Baltimore, MD 21218, USA*

³*Department of Physics and Astronomy, 4129 Frederick Reines Hall, University of California, Irvine, CA 92697, USA*

⁴*Departamento de Astronomia, IF, Universidade Federal do Rio Grande do Sul, CP 15051, 91501-970, Porto Alegre, RS, Brazil*

ABSTRACT

We use the James Webb Space Telescope (JWST) Mid-Infrared Instrument (MIRI) medium-resolution spectrometer (MRS) observations of the radio loud AGN host UGC 8782 to map the warm molecular and ionized gas kinematics. The data reveal outflows in the inner 2 kpc, seen in low ionization (traced by the [Ar II] 6.99 μm emission) and in warm molecular gas (traced by the H₂ rotational transitions), observed for the first time in an AGN host. We find a maximum mass-outflow rate of $4.90 \pm 2.04 M_{\odot} \text{ yr}^{-1}$ at ~ 900 pc from the nucleus for the warm outflow ($198 \text{ K} \leq T \leq 1000 \text{ K}$) and estimate and outflow rate of up to $1.22 \pm 0.51 M_{\odot} \text{ yr}^{-1}$ for the hotter gas phase ($T > 1000 \text{ K}$). These outflows can clear the entire nuclear reservoir of warm molecular gas in about 1 Myr. The derived kinetic power of the molecular outflows lead to coupling efficiencies of 2-5 percent of the AGN luminosity, way above the minimum expected to the AGN feedback be effective quenching the star formation.

Keywords: galaxies: active — galaxies: kinematics and dynamics — ISM: jets and outflows — quasars: individual (UGC 8782)

1. INTRODUCTION

Among the myriad challenges in constructing robust models of galaxy evolution, one glaring gap persists: the scarcity of galaxies at both ends of the mass spectrum during the later stages of cosmic history. This puzzling phenomenon presents a significant enigma in extragalactic astrophysics: Why are there so few galaxies of both low and high masses? The absence of galaxies at both mass ends indicates that our understanding of galaxy evolution remains incomplete, with numerous factors yet to be fully explored or discovered. Among these factors, supernova (Erb 2015; Chisholm et al. 2017) and ionization feedback (Bullock 2010; Brooks et al. 2013) emerges as crucial components, essential for suppressing the formation of stellar mass in galaxies at the low-mass end. At the high-mass end, supernova feedback is insufficient (Silk 2011), but the energy demands for removal or reheating the gas available for star formation can potentially be met by Active Galactic Nuclei (AGN). Indeed, numerous models have been developed to elucidate AGN feedback, demonstrating that even with low coupling efficiencies, AGN can exert a substantial impact on their host galaxies (e.g. Anglés-Alcázar et al. 2017; Almeida

et al. 2023). AGN-driven winds have the ability to reheat, expel or redistribute the gas within the galaxy. Because the AGN-driven winds are a multi-phase phenomenon, with a wide range of it is imperative to thoroughly examine each.

The molecular gas is the main driver of star formation (SF) (Kennicutt & Evans 2012) and AGN activity (Storchi-Bergmann & Schnorr-Müller 2019). Conventionally, it is common to separate molecular gas into three phases with well-defined tracers: (i) The cold gas, in which the temperatures reaches no more than 100 K. This phase is the densest gas phase and is commonly traced by (sub)millimeter transitions of molecules such as CO and HCN; (ii) The warm molecular gas phase, $100 \text{ K} \lesssim T \lesssim 1000 \text{ K}$, summing up to ~ 1 -30 percent of total molecular gas mass (Roussel et al. 2007). This specific gas phase can be traced by the rotational H₂ transitions seen in the mid-infrared (MIR); (iii) The hot molecular phase, $T \gtrsim 1000 \text{ K}$, mainly traced by the roto-vibrational H₂ transitions in the near-infrared. This gas phase represents only 10^{-7} – 10^{-5} of the mass of the cold molecular gas phase (Dale et al. 2005; Emonts et al. 2014; Pereira-Santaella et al. 2016). Spatially re-

solved observations of the structure and kinematics of both cold and hot molecular gas emissions in the central regions of galaxies have been meticulously obtained through ALMA and near-infrared integral field unit observations (Lamperti et al. 2022; Riffel et al. 2023b).

With the advent of JWST, it is now possible to conduct detailed studies of the warm molecular phase, in particular with the Mid-Infrared Instrument (MIRI) medium-resolution spectrometer (MRS). These studies reveal a wide range of interactions between different gas phases, as found for the Stephan’s Quintet, one of the first low-redshift system to undergo a detailed analysis (Appleton et al. 2023); molecular gas tracing the deceleration of the radio jets by interaction with the disk in NGC 7319 (Pereira-Santaella et al. 2022); detection of highly ionized outflows in a Compton-thick AGN (Álvarez-Márquez et al. 2023); the presence of warm molecular outflows in NGC 3256, a nearby starburst galaxies (Bohn et al. 2024), among others (e.g. García-Bernete et al. 2022; Hernandez et al. 2023; Armus et al. 2023; González-Alfonso et al. 2023; Francis et al. 2024; Vayner et al. 2024; U et al. 2022).

Spitzer telescope observations of nearby galaxies have revealed a significant excess of H_2 emission observed from the rotational transitions in AGN hosts compared to star-forming galaxies (Lambrides et al. 2019). Furthermore, the MIR H_2 emission lines are especially conspicuous in shocked gas (Hill & Zakamska 2014) and are predicted by numerical simulations to be valuable tools for investigating the warm molecular gas phase of galactic outflows (Richings & Faucher-Giguère 2018a,b). Moreover, the surplus of H_2 emission observed in AGN hosts correlates with optical shock tracers, such as $[O\text{I}]\lambda 6300$, offering observational evidence that H_2 MIR lines can be employed to observe gas shocked by AGN winds (Riffel et al. 2020). Besides the H_2 transitions, the MIR spectral range includes also shock tracers in partially ionized gas zones, such as $[\text{Fe}\text{II}]$ emission lines (Rodríguez-Ardila et al. 2004; Riffel et al. 2013; Koo et al. 2018), and emission lines from the fully ionized gas.

Here, we use JWST MIRI observations to map the gas kinematics in the $3.5 \times 3.5 \text{ kpc}^2$ central region of the radio-loud AGN, UGC 8782 (3C 293). This galaxy was selected from the sample of Riffel et al. (2020) as one of the objects with the largest H_2 emission excess (traced by the $H_2\text{S}(3) 9.665 \mu\text{m}/\text{PAH} 11.3 \mu\text{m}$ emission-line ratio) as well as the highest $[O\text{I}]\lambda 6300$ velocity dispersion and $[O\text{I}]\lambda 6300/H\alpha$ flux line ratio in their sample. This makes this galaxy an excellent candidate to host warm molecular gas outflows. UGC 8782 is located at a distance of $203.4 \pm 14.21 \text{ Mpc}$ (Albaret et al. 2017), host-

ing a radio loud AGN (e.g., Liu & Zhang 2002), and a double-double radio source with the outer lobes extending up to 200 kpc the northwest-southeast direction and inner lobes on a $\sim 4 \text{ kpc}$ scale aligned along the east-west direction (e.g., Machalski et al. 2016). Based on optical diagnostics, its nuclear activity is classified as a Low-Ionization Nuclear Emission Region (LINER, Véron-Cetty & Véron 2006) and optical images reveal dust filaments on scales from 100s of parsecs to a few kpc, associated with a previous merger event (e.g., Martel et al. 1999). UGC 8782 displays multi-gas phase outflows, observed in neutral hydrogen (Morganti et al. 2003; Mahony et al. 2013), and in ionized gas (Emonts et al. 2005; Mahony et al. 2016; Riffel et al. 2023a). These outflows are interpreted as being mechanically driven by the radio jet and the kinetic power of the ionized gas outflows is in the range of 1–3 per cent of the AGN bolometric luminosity (Riffel et al. 2023a). The cold molecular component of the outflows remains undetected thus far (Labiano et al. 2014) and here we report, for the first time, the observations of warm molecular outflows by studying the mid-infrared H_2 emission, using spatially resolved observations with JWST.

This paper is organized as follows: In Sec. 2 we describe the data and measurements, while Sec. 3 presents the results and discuss them. Sec. 4 summarizes our conclusions.

2. DATA AND MEASUREMENTS

The observations were performed with the JWST using the (Mid-Infrared Instrument (MIRI) Wells et al. 2015; Argyriou et al. 2023, medium-resolution spectrometer (MRS)) in the sub-bands Short and Long. We adopted a four point dither pattern, with 30 groups and a single integration for each dither position. We used the slow readout mode, which yields a total exposure time on source of 1 h 35m, and we obtain an additional 24 m of background exposure performed at the first dither position.

The science and background observations were processed using the JWST Science Calibration Pipeline (Bushouse et al. 2024), version 1.13.4, and reference file `jwst_1188.pmap`. After completing the initial data reduction steps, we process the cosmic ray files through a custom outlier detection script to remove residual outliers. To eliminate the resampling noise, a necessary step to fit the emission lines (Law et al. 2023), we reassign the spectrum of each spaxel to the integrated light within an aperture of 0.5 arcsec centered on the spaxel. The resulting spectrum is then renormalized by multiplying it by the ratio of the observed continuum to the integrated spectrum’s continuum at each wavelength. This

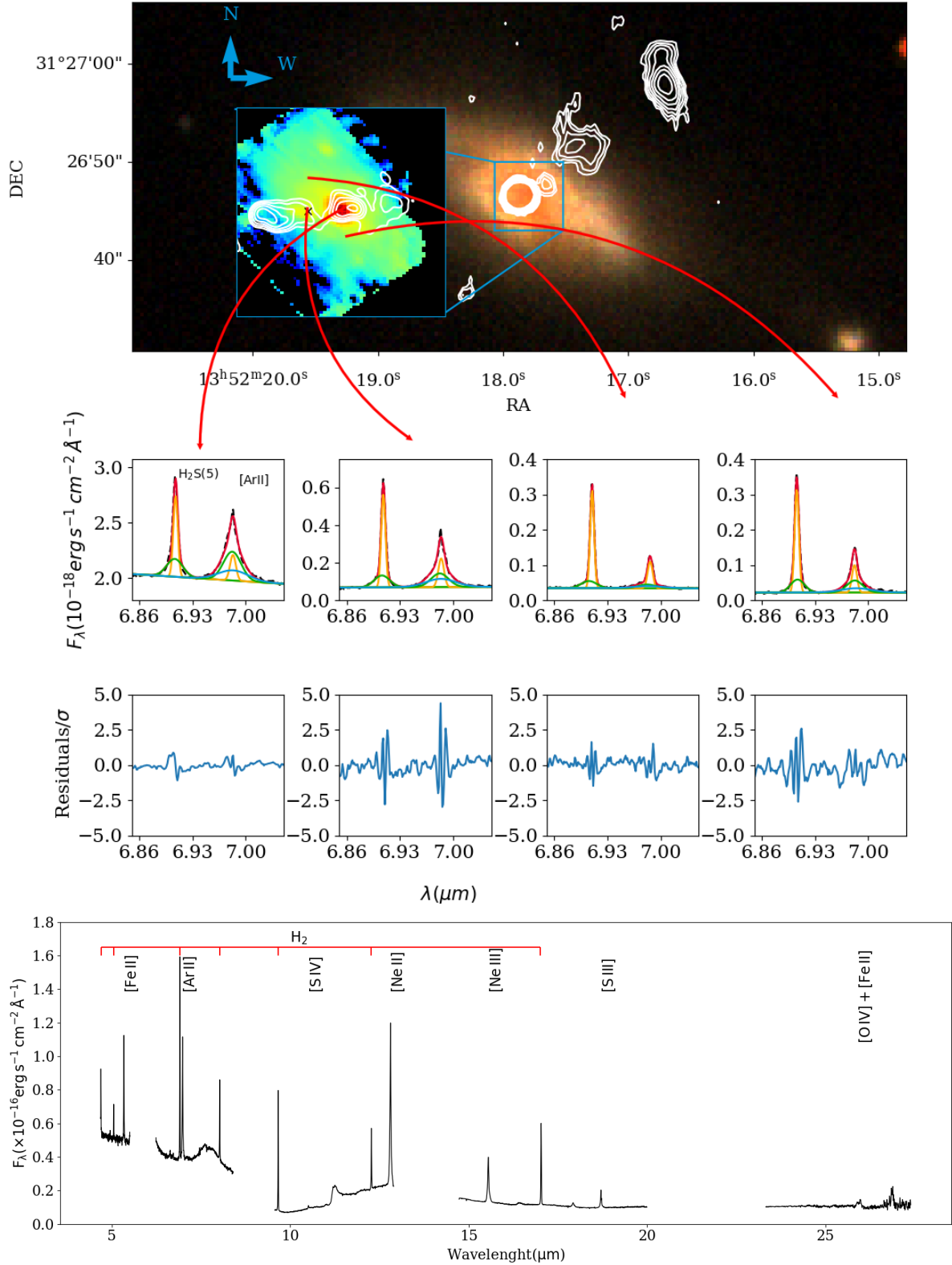


Figure 1. Sloan Digital Sky Survey RGB composition of UGC 8782. The white contours trace the radio-jet at 1.4GHz, obtained from VLA archive (Becker et al. (1995)). The zoomed in panel displays the JWST MIRI 7.0 μm continuum image. The white contours are from a L-Band (1.65 GHz) image from the e-Merlin archive. The position of the MIR emission peak is indicated by a + sign, while the \times shows the position of the optical nucleus. The plots show examples of fits of the emission lines for four positions, along with the residuals of the fits divided by the standard deviation of the nearby continuum. The bottom panel shows an integrated spectrum within a circular aperture of 1 arcsec around the nucleus.

approach does not significantly affect the amplitude and kinematics of the emission lines. A similar procedure is adopted by Perna et al. (2023) for processing NIRSPEC IFU data. The Background subtraction was performed using the master background subtraction method. In this process, a 1-D master background spectrum is derived from the background exposures and then projected into the 2-D space of the source data, to perform the subtraction. A detailed description of the observations and data reduction procedure will be provided in a forthcoming paper (Souza-Oliveira et al., in prep.).

The resulting data covers the spectral region 4.7-27 μm , excluding the Medium sub-band windows (5.49-6.24 μm , 8.39-9.57 μm , 12.88-14.74 μm and 20.00-23.36 μm). The mid-infrared spectrum of UGC 8782 is abundant in emission lines from the molecular gas (H_2 rotational transitions), as well as emission lines from ionized species such as [Fe II] 5.34 μm , [Ar II] 6.99 μm , [Ne II] 12.81 μm , [Ne III] 15.56 μm , [S III] 18.71 μm , and a few lines are quite fainter ([Si IV] 10.51 μm , [Fe II] 17.94 μm), as observed in the bottom panel of Fig. 1. Here, we focus our analysis in the H_2 rotational transitions, tracers of the warm molecular gas, and use the [Ar II] 6.99 μm as a tracer of the ionized gas emission. The angular resolution is about ~ 0.36 arcsec as obtained by measuring the FWHM of the flux distributions of the stars HD 192163 and HD 2811 at 7.0 μm , after processing the data following the same procedure used to obtain the datacube for UGC 8782.

We use the IFSCUBE Python package (Ruschel-Dutra et al. 2021) to fit the emission lines by Gaussian functions for each profile. We create the observed continuum by applying a double lowess smoothing for each spectral interval in the observed spectrum, using 30% and 10% of the data points in this order, followed by linear interpolation. Then, the emission lines are fitted using the continuum subtracted spectra. The H_2 lines are well reproduced by two Gaussian each, while the [Ar II] 6.99 μm , required an additional component to reproduce the line profile. The residuals from the fits for all lines are comparable to the noise in the continuum. They exceed 5σ of the continuum noise level in only 5% of the spaxels with measurements for H_2 S(5) and 3% for the [Ar II]. Examples of the fits are shown in Fig. 1 for four positions. The IFSCUBE code outputs a data cube including the best-fit parameters which are used to map the emission line flux distributions and kinematics.

3. RESULTS AND DISCUSSIONS

We find that the peak of the continuum emission in the MIR is shifted by ~ 0.6 arcsec to the west in relation to

the peak of optical emission, while the emission peaks of optical lines and the IR are co-spatial (Riffel et al. 2023a). The MIR emission peak is consistent with the position of the radio core. This is consistent with previous observations that reported a displacement between the optical center and the radio core in UGC 8782 (e.g. Emonts et al. 2005; Mahony et al. 2016) and is likely due to higher extinction in the optical continuum.

In Fig. 2, we present the flux distributions and kinematic maps for the $\text{H}_2\text{S}(5)$ 6.91 μm and [Ar II] 6.99 μm emission lines. The top panels show the results for the narrow component, attributed to the disk emission, while the middle panels show the resulting maps for the broad component, due the outflow. In addition, a very broad component is observed in [Ar II] (a fast outflow), with a median velocity dispersion of $\sigma \sim 860 \text{ km s}^{-1}$ and centroid velocity close to galaxy's systemic velocity. We do not show the maps for this component as it is very compact, extending to up to 0.8 arcsec from the MIR continuum peak, as seen in the bottom panels of Fig. 2. The disk component has extended emission over the whole MIRI-MRS field of view and gas kinematics consistent with a rotation pattern centered on the MIR nucleus.

The emission of the outflow component (bottom panels of Fig. 2) is spatially resolved (with FWHM of its flux distribution of about 2.4 times that of the PSF) and concentrated mostly around the MIR nucleus and radio core. In addition, we simulated a rotating disk convolved with the PSF to assess the impact of beam smearing on the observed line profiles, which was found to be negligible (refer to the Appendix A). This component is blue-shifted relative to the systemic velocity of the galaxy and presents σ values of up to $\sim 600 \text{ km s}^{-1}$. The median velocity and σ values are -70 km s^{-1} and 455 km s^{-1} for the [Ar II] and -50 km s^{-1} and 430 km s^{-1} for the H_2 , respectively. From the observed H_2 emission and kinematics, we derive the warm molecular gas outflow properties, for the first time, in UGC 8782.

We measure the gas mass and temperature using the transitions H_2 (0-0) S(1), H_2 (0-0) S(2), H_2 (0-0) S(3), H_2 (0-0) S(4) and H_2 (0-0) S(5), as our data does not include the higher order transitions, as well as the H_2 (0-0) S(0) transition. We correct the observed fluxes for extinction using a visual extinction of $A_V = 1.7$ mag, the mean value for the outflow component (Riffel et al. 2023a) and adopting the extinction law from Gordon et al. (2023).

To estimate the mass of the warm molecular gas, we assume that the gas lies in a temperatures distribution, with an optically thin gas. Given that a single temperature is rarely sufficient to reproduce the observed data

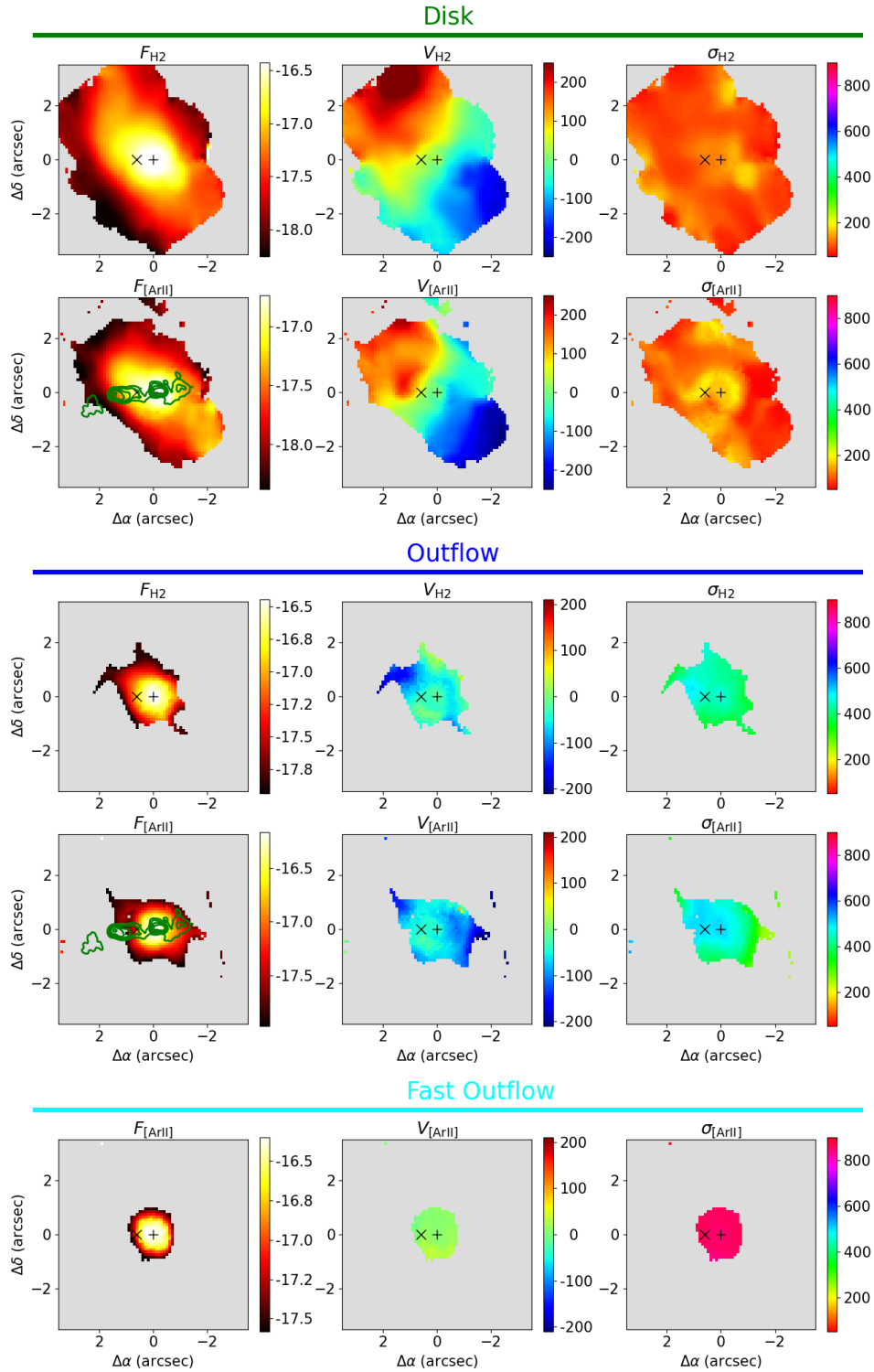


Figure 2. The top panels show the flux distribution in $\log_{10}(\text{erg s}^{-1}\text{cm}^{-2})$ (left), velocity field (center) and velocity dispersion map (right) for the narrow (disk) component of the H₂ S(1) (top) and [Ar II] 6.99 μm (bottom) emission lines. The + and × symbols mark the position of the MIR and optical continuum peaks, respectively. The gray regions correspond to locations where the emission lines are not detected with at least 3 sigma above the continuum noise. The green contours are from the L-Band (1.65 GHz) image from the e-Merlin archive. The middle panels show the results for the outflow component with the same nomenclature used for the disk component, while the bottom panels show the results for the fast outflow seen in [Ar II] 6.99 μm.

(e.g., Roussel et al. 2007; Higdon et al. 2006; Petric et al. 2018), we employ a power law approach to estimate the mass within a temperature interval $[T, T + dT]$ (Pereira-Santaella et al. 2014; Togi & Smith 2016). The column density N_T can be estimated from the column density of the J state N_J , given by

$$N_J = \int_{T_u}^{T_l} f(T) m T^{-n} dT, \quad (1)$$

where m is a normalization constant $m = N_T(n - 1)/(T_l^{1-n} - T_u^{1-n})$, $f(T)$ is the Boltzmann factor to the ortho states

$$f(T) = \frac{g_J e^{-E_J/k_B T}}{\sum_{J'=1}^{\text{ortho}} g_{J'} e^{-E_{J'}/k_B T}}. \quad (2)$$

$g_J = 3(2J + 1)$ is the degeneracy of the ortho J state and k_B is the Boltzmann constant. Following Landau & Lifshitz's (1991) and Huber & Herzberg (1979) the energy of the state can be obtained by

$$E_J = 85.35 \text{ K } k_B J(J+1) - 0.068 \text{ K } k_B J^2(J+1)^2. \quad (3)$$

The column density N_J can also be determine directly, by $N_J = 4\pi F_J/\Omega(\Delta E_{u-l} A_{u-l})$, ΔE_{u-l} is the energy of the transition, A_{u-l} is the Einstein coefficient of the considered transition, and Ω is the solid angle of observation. Replacing N_J in Eq. 1, we obtain that the total column density at the ortho state by:

$$N_T = \frac{4\pi F_J(T_l^{1-n} - T_u^{1-n})}{\Omega(\Delta E_{u-l} A_{u-l})(n-1) \int_{T_u}^{T_l} f(T) T^{-n} dT}. \quad (4)$$

To estimate the gas mass, we need to determine the power-law index (n), the upper (T_u) and lower (T_l) temperature limits. This can be done by dividing N_J for the column density of a reference state, e.g. N_3 ,

$$\frac{N_J/g_J}{N_3/g_3} = \frac{\int_{T_u}^{T_l} e^{-E_J/k_B T} T^{-n} dT}{\int_{T_u}^{T_l} e^{-E_3/k_B T} T^{-n} dT}. \quad (5)$$

Following Yuan & Neufeld (2011), we use $T_u = 5000\text{K}$ to include the hot molecular phase, and vary the parameter space of T_l and n in order to minimize the equation above. The resulting models for the disk and outflow components are shown in Fig. 3. The disk component is well reproduced with $n = 4.84$ in a temperature range from 134 to 5000 K, similarly to what was found by (Togi & Smith 2016), using Spitzer data. For the outflow, we find $n = 4.26$ within a temperature range of 198–5000 K. This shallower slope for the outflow component is consistent with shock heated gas cooling through the emission of the higher J transitions (Appleton et al. 2017).

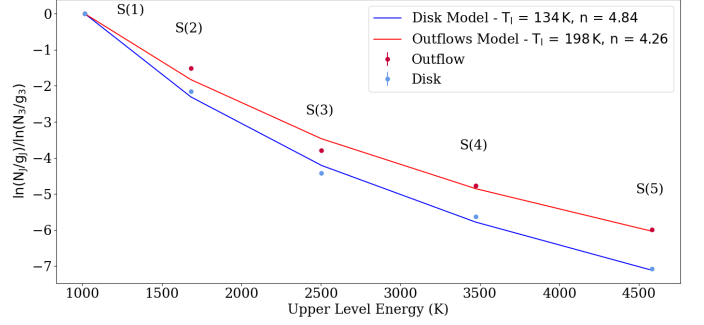


Figure 3. Excitation diagrams for the outflow and disk components. The y -axis shows the population number of the J state divided by the degeneracy of the state and normalized by the $J=3$ state, while the x -axis shows the upper level energy. The red line, describes the power-law model fitted at the outflow component, while the blue line represents the disk.

Finally, the mass of gas is obtained by

$$M = (4/3)m_{\text{H}_2} N_T \Omega D^2, \quad (6)$$

where m_{H_2} is the mass of the H_2 molecule and ΩD^2 is the area of the encompassed region. The $4/3$ factor is used to account for the mass of the molecule at the para state, considering a ortho to para ratio of 3. We estimate the masses and outflow properties for the two phases the warm (198K-1000K) and the hot (1000K-5000 K). We obtain masses of $(7.02 \pm 2.57) \times 10^6 M_\odot$ and $(1.95 \pm 0.71) \times 10^5 M_\odot$, for the warm and the hot gas phases, respectively.

To estimate the mass outflow rate (\dot{M}) and kinetic power (\dot{K}) of the outflow, we adopt a spherical shell outflow geometry, for which

$$\dot{M} = \frac{M_{\text{out},\Delta R} V_{\text{out},\Delta R}}{\Delta R}, \quad (7)$$

where $M_{\text{out},\Delta R}$ is the outflowing mass for each shell, with width of $\Delta R = 0.3''$ (close to the angular resolution), we also use the $V_{\text{out},\Delta R} = v_{98} = |\langle V_{\text{wind}} \rangle_{\Delta R}| + 2\langle \sigma_{\text{wind}} \rangle_{\Delta R}$ as commonly done in the literature (Rupke & Veilleux 2013; Dall'Agno de Oliveira et al. 2021). The median velocity of the molecular outflows in UGC 8782 is $\sim 900 \text{ km s}^{-1}$. This value is smaller than the escape velocity of the galaxy, which is $\sim 1130 \text{ km s}^{-1}$, implying that the outflows are only capable of redistributing gas within the galaxy. However, it will still be available for further star formation.

The kinetic power of the outflow for each shell is estimated as

$$\dot{K} = \frac{M_{\text{out},\Delta R} (V_{\text{out},\Delta R})^3}{2\Delta R}. \quad (8)$$

Fig. 4 presents the radial profiles of the mass-outflow rate (top panel) and kinetic power (bottom panel) for

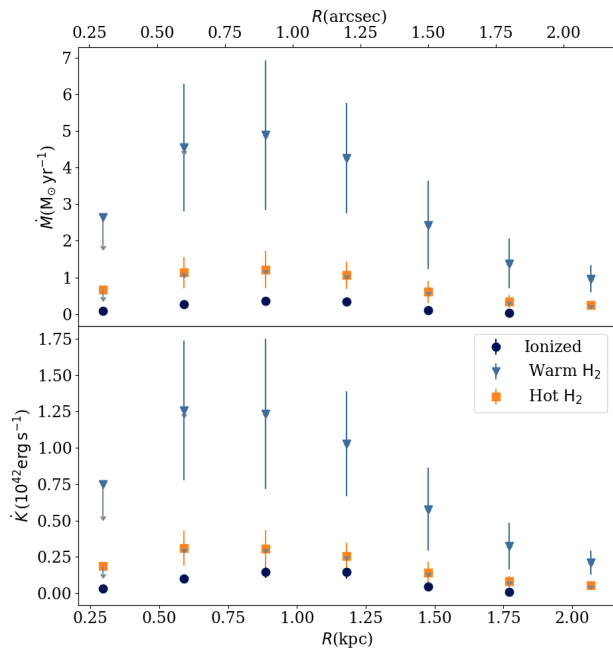


Figure 4. Radial plots for the mass-outflow rate (top panel) and kinetic power of the outflows (bottom panel). The dark blue points represent the ionized outflows, warm H₂ is shown in light blue and the hot H₂ is shown as orange squares. The arrows in the first radial bin show the minimum values of the outflow properties, after correcting for the PSF scatter if an unresolved outflow is present. For bins further from the nucleus, the PSF contribution is negligible ($\lesssim 2\%$), so the arrows are not shown.

the warm and hot molecular outflows, in bins of 0.3 arcsec. We also include, for comparison, the radial profiles for the ionized gas outflows based on the H α emission, using the data from Riffel et al. (2023a) and the same methodology described here, however with a seeing of ~ 0.75 arcsec. The maximum outflow rate of $4.90 \pm 2.04 M_{\odot} \text{ yr}^{-1}$ is seen in the warm phase at ~ 900 pc from the nucleus, whilst the hot counterpart presents a lower contribution, of $1.22 \pm 0.51 M_{\odot} \text{ yr}^{-1}$. We estimate the contribution of scattered light from the nucleus to the derived mass outflow rates by scaling the flux of the broad component with the observed PSF for the star HD 2811, processed in the same way as the science data. We find a contribution of up to 30 % for the central bin, and contributions lower than 2 % for larger distances from the nucleus. The downward-pointing arrows in the first radial bin show the values after correcting for the PSF scatter if an unresolved outflow is present.

Given the AGN bolometric luminosity of $L_{\text{bol}} = (2.5 - 7.2) \times 10^{43} \text{ erg s}^{-1}$ (Riffel et al. 2023a), the molecular outflow demonstrates maximum kinetic coupling efficiencies (ϵ) ranging from 2–5% of the AGN luminosity, the kinetic power of the hot and warm phase are respec-

tively $1.26 \times 10^{42} \text{ erg s}^{-1}$ and $3.12 \times 10^{41} \text{ erg s}^{-1}$. This range far surpasses the minimum ϵ required for effective AGN feedback in suppressing star formation (Hopkins & Elvis 2010), particularly when considering the potential presence of a cold molecular gas reservoir that may also contribute to the outflow. Nevertheless, the outflows in UGC 8782 are likely mechanically driven by the radio jet, as the kinetic power of the outflow is one order of magnitude lower than the object’s radio source power of $(2 - 4) \times 10^{43} \text{ erg s}^{-1}$ (Lanz et al. 2015). Considering a constant outflow rate the warm and hot H₂ gas reservoir would be depleted in around ~ 1 Myr.

4. CONCLUSIONS

We reported, for the first time, the observations of warm molecular gas outflows from the AGN of UGC 8782. We find that the mass outflow rate in warm molecular gas is substantially higher than that observed in ionized gas across all radii, with coupling efficiencies exceeding the minimum required for AGN feedback to be effective in quenching star formation. The observed molecular outflows in UGC 8782 of up to $\sim 6 M_{\odot} \text{ yr}^{-1}$ are able of redistributing all the warm molecular gas available in the inner 2 kpc of the UGC 8782 in only ~ 1 Myr.

ACKNOWLEDGMENTS

We would like to express our gratitude to an anonymous referee for their valuable comments that helped us improve this work. Additionally, we extend our thanks to the e-Merlin support staff for their assistance in retrieving the data from their archive, and to Rob Beswick for providing additional data. HCPS and GLSO thank the financial support from Coordenação de Aperfeiçoamento de Pessoal de Nível Superior - Brasil (CAPES) - Finance Code 001. RAR acknowledges the support from Conselho Nacional de Desenvolvimento Científico e Tecnológico (CNPq; Proj. 303450/2022-3, 403398/2023-1, & 441722/2023-7), Fundação de Amparo à pesquisa do Estado do Rio Grande do Sul (FAPERGS; Proj. 21/2551-0002018-0), and CAPES (Proj. 88887.894973/2023-00). RR and TSB acknowledge the support from CNPq and FAPERGS. M.B. acknowledges funding support from NASA Astrophysics Data Analysis Program (ADAP) grant No. 80NSSC23K0750 and STScI grant JWST-GO-01717.001-A, which was provided by NASA through a grant from the Space Telescope Science Institute, which is operated by the Association of Universities for Research in Astronomy, Inc., under NASA contract NAS 5-03127. M.B. is also grateful to the IAU’s Gruber Foundation Fellowship Program for the financial support.

DATA AVAILABILITY

The data used in this work are part of the JWST cycle 1 project (ID 1928). The complete dataset can be accessed at the Mikulski Archive for Space Telescopes (MAST) platform at the Space Telescope Science Institute, through [10.17909/tazj-hp44](https://doi.org/10.17909/tazj-hp44).

Facilities: JWST (MIRI MRS), Gemini (GMOS-IFU) e-MERLIN, MAST, NED.

Software: ASTROPY (Astropy Collaboration et al. 2022), IFSCUBE (Ruschel-Dutra et al. 2021), JWST Science Calibration (Bushouse et al. 2024), Matplotlib (Hunter 2007), QFitsView (Ott 2012), SciPy (Virtanen et al. 2020).

APPENDIX

A. BEAM SMEARING

The emission line profiles from distinct regions of a rotating disk component merge or blend together within the same resolution element, a effect known as beam smearing (e.g., Swaters et al. 2009). Consequently, an unresolved disk component can produce a single observed emission line profile that appears to have contributions from multiple underlying velocity components. This effect occurs because the spatial resolution of the observation is insufficient to distinguish between the different line-of-sight velocities present across the disk.

In order to evaluate the beam-smearing effect, we simulate a data cube in which the velocity field is given by a simple analytical model from Bertola et al. (1991), with a projected velocity amplitude of 200 km s^{-1} similar to the observed value. The $\text{H}_2 \text{S}(5)$, $6.91 \mu\text{m}$ emission line profile at each spaxel is represented by a Gaussian function with the flux decreasing with the distance from the nucleus and with a constant velocity dispersion of 100 km s^{-1} . The continuum emission is modeled by a power-law function, which decreases radially. Additionally, we include a random noise component that matches the observed noise level of the datacube. Then, we convoluted the data cube with the JWST PSF, represented by the flux distribution of the star HD 2811.

In Figure 5 we show the results of this toy model. The upper maps show the velocity field (left) and the emission-line flux distribution (right) before (top) and after (bottom) the convolution with the PSF, whilst the bottom plots show examples of the line profiles at the nuclear spaxel (top left), two spaxels along the major axis of the disk (top right) and (bottom left) and for an integrated aperture of 0.3 arcsec radius (bottom right). As can be observed from this figure, the line profiles before and after the convolution of the model with the PSF are similar, indicating that the effect of beam smearing is negligible.

REFERENCES

- Albareti, F. D., Allende Prieto, C., Almeida, A., et al. 2017, *ApJS*, 233, 25, doi: [10.3847/1538-4365/aa8992](https://doi.org/10.3847/1538-4365/aa8992)
- Almeida, I., Nemmen, R., & Riffel, R. A. 2023, *MNRAS*, 526, 217, doi: [10.1093/mnras/stad2673](https://doi.org/10.1093/mnras/stad2673)
- Álvarez-Márquez, J., Labiano, A., Guillard, P., et al. 2023, *A&A*, 672, A108, doi: [10.1051/0004-6361/202244880](https://doi.org/10.1051/0004-6361/202244880)
- Anglés-Alcázar, D., Davé, R., Faucher-Giguère, C.-A., Özel, F., & Hopkins, P. F. 2017, *MNRAS*, 464, 2840, doi: [10.1093/mnras/stw2565](https://doi.org/10.1093/mnras/stw2565)
- Appleton, P. N., Guillard, P., Togi, A., et al. 2017, *ApJ*, 836, 76, doi: [10.3847/1538-4357/836/1/76](https://doi.org/10.3847/1538-4357/836/1/76)
- Appleton, P. N., Guillard, P., Emonts, B., et al. 2023, *ApJ*, 951, 104, doi: [10.3847/1538-4357/accc2a](https://doi.org/10.3847/1538-4357/accc2a)
- Argyriou, I., Glasse, A., Law, D. R., et al. 2023, *A&A*, 675, A111, doi: [10.1051/0004-6361/202346489](https://doi.org/10.1051/0004-6361/202346489)
- Armus, L., Lai, T., U, V., et al. 2023, *ApJL*, 942, L37, doi: [10.3847/2041-8213/acac66](https://doi.org/10.3847/2041-8213/acac66)
- Astropy Collaboration, Price-Whelan, A. M., Lim, P. L., et al. 2022, *apj*, 935, 167, doi: [10.3847/1538-4357/ac7c74](https://doi.org/10.3847/1538-4357/ac7c74)
- Becker, R. H., White, R. L., & Helfand, D. J. 1995, *ApJ*, 450, 559, doi: [10.1086/176166](https://doi.org/10.1086/176166)
- Bertola, F., Bettoni, D., Danziger, J., et al. 1991, *ApJ*, 373, 369, doi: [10.1086/170058](https://doi.org/10.1086/170058)
- Bohn, T., Inami, H., Togi, A., et al. 2024, arXiv e-prints, arXiv:2403.14751, doi: [10.48550/arXiv.2403.14751](https://doi.org/10.48550/arXiv.2403.14751)
- Brooks, A. M., Kuhlen, M., Zolotov, A., & Hooper, D. 2013, *ApJ*, 765, 22, doi: [10.1088/0004-637X/765/1/22](https://doi.org/10.1088/0004-637X/765/1/22)
- Bullock, J. S. 2010, arXiv e-prints, arXiv:1009.4505, doi: [10.48550/arXiv.1009.4505](https://doi.org/10.48550/arXiv.1009.4505)
- Bushouse, H., Eisenhamer, J., Dencheva, N., et al. 2024, JWST Calibration Pipeline, 1.14.0, Zenodo, doi: [10.5281/zenodo.10870758](https://doi.org/10.5281/zenodo.10870758)
- Chisholm, J., Tremonti, C. A., Leitherer, C., & Chen, Y. 2017, *MNRAS*, 469, 4831, doi: [10.1093/mnras/stx1164](https://doi.org/10.1093/mnras/stx1164)

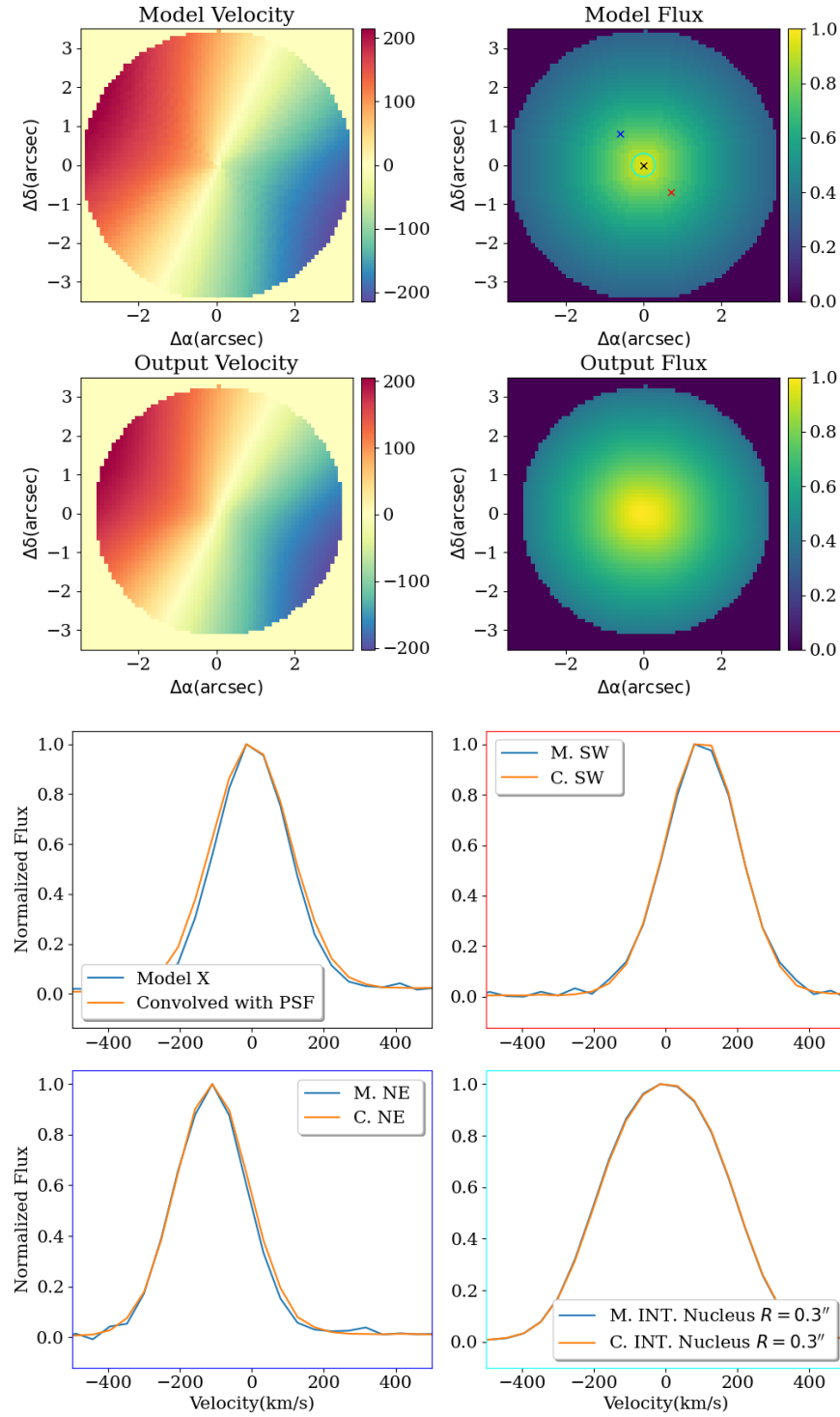


Figure 5. The maps show the models for the velocity (left) and the emission-line flux distribution (right) before (top) and after (bottom) the convolution with PSF. Examples of line profiles before (in blue) and after (orange) the convolution with the PSF are shown at the bottom plots, for the positions indicated in the model flux map.

- Dale, D. A., Sheth, K., Helou, G., Regan, M. W., & Hüttemeister, S. 2005, *AJ*, 129, 2197, doi: [10.1086/429134](https://doi.org/10.1086/429134)
- Dall’Agnol de Oliveira, B., Storchi-Bergmann, T., Kraemer, S. B., et al. 2021, *MNRAS*, 504, 3890, doi: [10.1093/mnras/stab1067](https://doi.org/10.1093/mnras/stab1067)
- Emonts, B. H. C., Morganti, R., Tadhunter, C. N., et al. 2005, *MNRAS*, 362, 931, doi: [10.1111/j.1365-2966.2005.09354.x](https://doi.org/10.1111/j.1365-2966.2005.09354.x)
- Emonts, B. H. C., Piqueras-López, J., Colina, L., et al. 2014, *A&A*, 572, A40, doi: [10.1051/0004-6361/201423805](https://doi.org/10.1051/0004-6361/201423805)
- Erb, D. K. 2015, *Nature*, 523, 169, doi: [10.1038/nature14454](https://doi.org/10.1038/nature14454)
- Francis, L., van Gelder, M. L., van Dishoeck, E. F., et al. 2024, arXiv e-prints, arXiv:2401.06880, doi: [10.48550/arXiv.2401.06880](https://doi.org/10.48550/arXiv.2401.06880)
- García-Bernete, I., Rigopoulou, D., Alonso-Herrero, A., et al. 2022, *A&A*, 666, L5, doi: [10.1051/0004-6361/202244806](https://doi.org/10.1051/0004-6361/202244806)
- González-Alfonso, E., García-Bernete, I., Pereira-Santaella, M., et al. 2023, arXiv e-prints, arXiv:2312.04914, doi: [10.48550/arXiv.2312.04914](https://doi.org/10.48550/arXiv.2312.04914)
- Gordon, K. D., Clayton, G. C., Declair, M., et al. 2023, *ApJ*, 950, 86, doi: [10.3847/1538-4357/accb59](https://doi.org/10.3847/1538-4357/accb59)
- Hernandez, S., Jones, L., Smith, L. J., et al. 2023, *ApJ*, 948, 124, doi: [10.3847/1538-4357/acc837](https://doi.org/10.3847/1538-4357/acc837)
- Higdon, S. J. U., Armus, L., Higdon, J. L., Soifer, B. T., & Spoon, H. W. W. 2006, *ApJ*, 648, 323, doi: [10.1086/505701](https://doi.org/10.1086/505701)
- Hill, M. J., & Zakamska, N. L. 2014, *MNRAS*, 439, 2701, doi: [10.1093/mnras/stu123](https://doi.org/10.1093/mnras/stu123)
- Hopkins, P. F., & Elvis, M. 2010, *MNRAS*, 401, 7, doi: [10.1111/j.1365-2966.2009.15643.x](https://doi.org/10.1111/j.1365-2966.2009.15643.x)
- Huber, K. P., & Herzberg, G. 1979, *Constants of diatomic molecules* (Boston, MA: Springer US), 8–689, doi: [10.1007/978-1-4757-0961-2_2](https://doi.org/10.1007/978-1-4757-0961-2_2)
- Hunter, J. D. 2007, *Computing in Science & Engineering*, 9, 90, doi: [10.1109/MCSE.2007.55](https://doi.org/10.1109/MCSE.2007.55)
- Kennicutt, R. C., & Evans, N. J. 2012, *ARA&A*, 50, 531, doi: [10.1146/annurev-astro-081811-125610](https://doi.org/10.1146/annurev-astro-081811-125610)
- Koo, B.-C., Kim, H.-J., Lee, Y.-H., et al. 2018, *ApJ*, 866, 139, doi: [10.3847/1538-4357/aae20e](https://doi.org/10.3847/1538-4357/aae20e)
- Labiano, A., García-Burillo, S., Combes, F., et al. 2014, *A&A*, 564, A128, doi: [10.1051/0004-6361/201323123](https://doi.org/10.1051/0004-6361/201323123)
- Lambrides, E. L., Petric, A. O., Tchernyshyov, K., Zakamska, N. L., & Watts, D. J. 2019, *MNRAS*, 487, 1823, doi: [10.1093/mnras/stz1316](https://doi.org/10.1093/mnras/stz1316)
- Lamperti, I., Pereira-Santaella, M., Perna, M., et al. 2022, *A&A*, 668, A45, doi: [10.1051/0004-6361/202244054](https://doi.org/10.1051/0004-6361/202244054)
- Landau, L. D., & Lifshitz, E. M. 1991, *Quantum mechanics : non-relativistic theory*
- Lanz, L., Ogle, P. M., Evans, D., et al. 2015, *ApJ*, 801, 17, doi: [10.1088/0004-637X/801/1/17](https://doi.org/10.1088/0004-637X/801/1/17)
- Law, D. R., E. Morrison, J., Argyriou, I., et al. 2023, *AJ*, 166, 45, doi: [10.3847/1538-3881/acdddc](https://doi.org/10.3847/1538-3881/acdddc)
- Liu, F. K., & Zhang, Y. H. 2002, *A&A*, 381, 757, doi: [10.1051/0004-6361:20011572](https://doi.org/10.1051/0004-6361:20011572)
- Machalski, J., Jamrozy, M., Stawarz, L., & Weżgowiec, M. 2016, *A&A*, 595, A46, doi: [10.1051/0004-6361/201629249](https://doi.org/10.1051/0004-6361/201629249)
- Mahony, E. K., Morganti, R., Emonts, B. H. C., Oosterloo, T. A., & Tadhunter, C. 2013, *MNRAS*, 435, L58, doi: [10.1093/mnrasl/slt094](https://doi.org/10.1093/mnrasl/slt094)
- Mahony, E. K., Oonk, J. B. R., Morganti, R., et al. 2016, *MNRAS*, 455, 2453, doi: [10.1093/mnras/stv2456](https://doi.org/10.1093/mnras/stv2456)
- Martel, A. R., Baum, S. A., Sparks, W. B., et al. 1999, *ApJS*, 122, 81, doi: [10.1086/313205](https://doi.org/10.1086/313205)
- Morganti, R., Oosterloo, T. A., Emonts, B. H. C., van der Hulst, J. M., & Tadhunter, C. N. 2003, *ApJL*, 593, L69, doi: [10.1086/378219](https://doi.org/10.1086/378219)
- Ott, T. 2012, QFitsView: FITS file viewer, Astrophysics Source Code Library, record ascl:1210.019. <http://ascl.net/1210.019>
- Pereira-Santaella, M., Spinoglio, L., van der Werf, P. P., & Piqueras López, J. 2014, *A&A*, 566, A49, doi: [10.1051/0004-6361/201423430](https://doi.org/10.1051/0004-6361/201423430)
- Pereira-Santaella, M., Colina, L., García-Burillo, S., et al. 2016, *A&A*, 594, A81, doi: [10.1051/0004-6361/201628875](https://doi.org/10.1051/0004-6361/201628875)
- Pereira-Santaella, M., Álvarez-Márquez, J., García-Bernete, I., et al. 2022, *A&A*, 665, L11, doi: [10.1051/0004-6361/202244725](https://doi.org/10.1051/0004-6361/202244725)
- Perna, M., Arribas, S., Marshall, M., et al. 2023, *A&A*, 679, A89, doi: [10.1051/0004-6361/202346649](https://doi.org/10.1051/0004-6361/202346649)
- Petric, A. O., Armus, L., Flagey, N., et al. 2018, *AJ*, 156, 295, doi: [10.3847/1538-3881/aaca35](https://doi.org/10.3847/1538-3881/aaca35)
- Richings, A. J., & Faucher-Giguère, C.-A. 2018a, *MNRAS*, 474, 3673, doi: [10.1093/mnras/stx3014](https://doi.org/10.1093/mnras/stx3014)
- . 2018b, *MNRAS*, 478, 3100, doi: [10.1093/mnras/sty1285](https://doi.org/10.1093/mnras/sty1285)
- Riffel, R., Rodríguez-Ardila, A., Aleman, I., et al. 2013, *MNRAS*, 430, 2002, doi: [10.1093/mnras/stt026](https://doi.org/10.1093/mnras/stt026)
- Riffel, R. A., Riffel, R., Bianchin, M., et al. 2023a, *MNRAS*, 521, 3260, doi: [10.1093/mnras/stad776](https://doi.org/10.1093/mnras/stad776)
- Riffel, R. A., Zakamska, N. L., & Riffel, R. 2020, *MNRAS*, 491, 1518, doi: [10.1093/mnras/stz3137](https://doi.org/10.1093/mnras/stz3137)
- Riffel, R. A., Storchi-Bergmann, T., Riffel, R., et al. 2023b, *MNRAS*, 521, 1832, doi: [10.1093/mnras/stad599](https://doi.org/10.1093/mnras/stad599)
- Rodríguez-Ardila, A., Pastoriza, M. G., Viegas, S., Sigut, T. A. A., & Pradhan, A. K. 2004, *A&A*, 425, 457, doi: [10.1051/0004-6361:20034285](https://doi.org/10.1051/0004-6361:20034285)
- Roussel, H., Helou, G., Hollenbach, D. J., et al. 2007, *ApJ*, 669, 959, doi: [10.1086/521667](https://doi.org/10.1086/521667)

- Rupke, D. S. N., & Veilleux, S. 2013, *ApJ*, 768, 75,
doi: [10.1088/0004-637X/768/1/75](https://doi.org/10.1088/0004-637X/768/1/75)
- Ruschel-Dutra, D., Storchi-Bergmann, T., Schnorr-Müller, A., et al. 2021, *MNRAS*, 507, 74,
doi: [10.1093/mnras/stab2058](https://doi.org/10.1093/mnras/stab2058)
- Silk, J. 2011, in *Tracing the Ancestry of Galaxies*, ed. C. Carignan, F. Combes, & K. C. Freeman, Vol. 277, 273–281, doi: [10.1017/S1743921311022939](https://doi.org/10.1017/S1743921311022939)
- Storchi-Bergmann, T., & Schnorr-Müller, A. 2019, *Nature Astronomy*, 3, 48, doi: [10.1038/s41550-018-0611-0](https://doi.org/10.1038/s41550-018-0611-0)
- Swaters, R. A., Sancisi, R., van Albada, T. S., & van der Hulst, J. M. 2009, *A&A*, 493, 871,
doi: [10.1051/0004-6361:200810516](https://doi.org/10.1051/0004-6361:200810516)
- Togi, A., & Smith, J. D. T. 2016, *ApJ*, 830, 18,
doi: [10.3847/0004-637X/830/1/18](https://doi.org/10.3847/0004-637X/830/1/18)
- U, V., Lai, T., Bianchin, M., et al. 2022, *ApJL*, 940, L5,
doi: [10.3847/2041-8213/ac961c](https://doi.org/10.3847/2041-8213/ac961c)
- Vayner, A., Zakamska, N. L., Ishikawa, Y., et al. 2024, *ApJ*, 960, 126, doi: [10.3847/1538-4357/ad0be9](https://doi.org/10.3847/1538-4357/ad0be9)
- Véron-Cetty, M. P., & Véron, P. 2006, *A&A*, 455, 773,
doi: [10.1051/0004-6361:20065177](https://doi.org/10.1051/0004-6361:20065177)
- Virtanen, P., Gommers, R., Oliphant, T. E., et al. 2020, *Nature Methods*, 17, 261, doi: [10.1038/s41592-019-0686-2](https://doi.org/10.1038/s41592-019-0686-2)
- Wells, M., Pel, J. W., Glasse, A., et al. 2015, *PASP*, 127, 646, doi: [10.1086/682281](https://doi.org/10.1086/682281)
- Yuan, Y., & Neufeld, D. A. 2011, *ApJ*, 726, 76,
doi: [10.1088/0004-637X/726/2/76](https://doi.org/10.1088/0004-637X/726/2/76)